


 Cite this: *RSC Adv.*, 2020, **10**, 19720

Deciphering the selectivity of inhibitor MKC9989 towards residue K907 in IRE1 α ; a multiscale *in silico* approach

Sayyed Jalil Mahdizadeh, Antonio Carlesso and Leif A. Eriksson *

The selectivity of the ligand MKC9989, as inhibitor of the Inositol-Requiring Enzyme 1 α (IRE1 α) transmembrane kinase/ribonuclease protein, towards the residue K907 in the context of Schiff base formation, has been investigated by employing an array of *in silico* techniques including Multi-Conformation Continuum Electrostatics (MCCE) simulations, Quantum Mechanics/Molecular Mechanics (QM/MM) calculations, covalent docking, and Molecular Dynamics (MD) simulations. According to the MCCE results, K907 displays the lowest pK_a value among all 23 lysine residues in IRE1 α . The MMCE simulations also indicate a critical interaction between K907 and D885 within the hydrophobic pocket which increases significantly at low protein dielectric constants. The QM/MM calculations reveal a spontaneous proton transfer from K907 to D885, consistent with the low pK_a value of K907. A Potential Energy Surface (PES) scan confirms the lack of energy barrier and transition state associated with this proton transfer reaction. Covalent docking and MD simulations verify that the protein pocket containing K907 can effectively stabilize the inhibitor by strong π - π and hydrogen bonding interactions. In addition, Radial Distribution Function (RDF) analysis shows that the imine group formed in the chemical reaction between MKC9989 and K907 is inaccessible to water molecules and thus the probability of imine hydrolysis is almost zero. The results of the current study explain the high selectivity of the MKC9989 inhibitor towards the K907 residue of IRE1 α .

 Received 28th February 2020
 Accepted 14th May 2020

DOI: 10.1039/d0ra01895c

rsc.li/rsc-advances

1. Introduction

Inositol-Requiring Enzyme 1 α (IRE1 α , hereafter IRE1) is a transmembrane endoplasmic reticulum (ER) bound bifunctional kinase and endoribonuclease protein crucial for the unfolded protein response (UPR) signaling. Upon ER stress, IRE1 homodimerizes, trans-autophosphorylates and oligomerizes, resulting in endoribonuclease activity with the excision of a 26 nucleotide intron from the X-box binding protein 1 (XBP1) mRNA.^{1,2} The mature form of XBP1s initiates the gene response to ER stress.³⁻⁵

UPR signaling is a promising target for the treatment of numerous diseases⁶ and targeting IRE1 activity, the most conserved sensor of the UPR, could elucidate the molecular mechanism of these complex signaling pathways. An inhibitor called MKC9989, able to target the RNase domain, has been developed by using a series of *in silico*, *in vitro* and *in vivo* data.⁷⁻⁹

From a functional point of the view, the MKC9989 inhibitor (Fig. 1) belongs to a series of IRE1 RNase inhibitors termed hydroxy aryl aldehydes (HAA) where the aldehyde moiety reacts chemically with the amine side chain of K907 through a Schiff base reaction.^{7,9} The molecular mechanism that can rationalize

the high selectivity specifically towards K907 out of the total 23 lysine residues is not yet well-understood. In the current work, complementing our previous study,¹⁰ we have conducted an in-depth investigation of this phenomenon.

To properly address the high selectivity of MKC9989 towards residue K907, we have considered different factors before and after the Schiff base formation, such as the capability of the lysine residues to be engaged in Schiff base reaction and the stability of the newly formed Schiff base. The most critical prerequisites for Schiff base formation is that the side chain amine group of lysine should be in its uncharged (deprotonated or neutral) state¹¹ to be able to nucleophilically attack the carbonyl group of MKC9989.⁷ Hence, the pK_a value of the lysine plays a crucial role for its reactivity toward Schiff base formation.¹² Another important factor is the capability of the receptor pocket environment in stabilizing the newly bound inhibitor.¹³ In this context, water accessibility to the imine group is an important parameter, since these can be easily hydrolyzed in the presence of water through a reverse Schiff base reaction.¹⁴

pK_a is a quantity that describes the amount of free energy change of a residue during the protonation process at a given pH.¹⁵ At neutral pH, the pK_a of an isolated lysine in water is 10.4,¹⁶ thus the side chain amine group would be protonated. However, in a protein, the microenvironment properties around

Department of Chemistry and Molecular Biology, University of Gothenburg, 405 30 Göteborg, Sweden. E-mail: leif.eriksson@chem.gu.se; Tel: +46 317869117



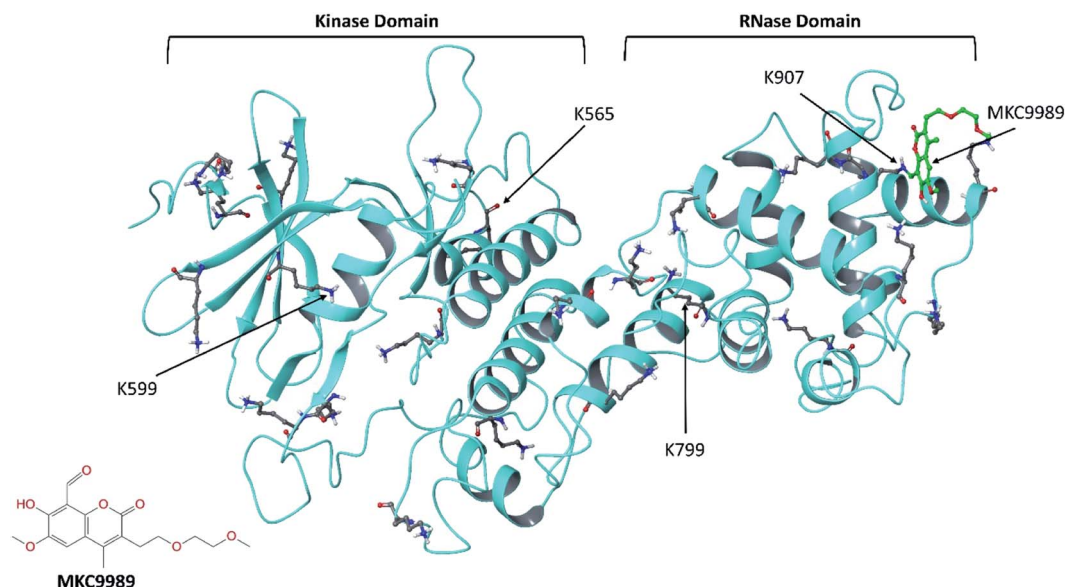


Fig. 1 The crystallographic structure of the cytosolic domain of IRE1 (PDB code: 4PL3) with the inhibitor MKC9989 covalently bound to residue K907 in the RNase domain. The protein backbone and all 23 lysine residues are shown in ribbon and ball-and-stick representation, respectively. The inset picture is the 2D molecular structure of MKC9989.

each residue can significantly alter its pH dependence towards protonation, mainly by electrostatic interactions, which results in significant shifts in pK_a values.¹⁷ It has been demonstrated that a pK_a shift of just one pH unit may have a large impact on the conformational change and biological activity of biomolecules.¹⁶ Antosiewicz *et al.*¹⁸ demonstrated that it is almost impossible to estimate reasonable values of pK_a for a fully rigid protein, especially with dielectric constants smaller than 20. The explicit motions of side chains can be considered in MD simulation with a predefined protonation state and by averaging the pK_a values over each structure throughout the trajectory.^{19,20} While this strategy seems efficient, it however ignores the energy difference between configurations in the MD trajectory, which in turn contributes to the free energy change of protonation.¹⁶

Herein, the Multi-Conformation Continuum Electrostatics (MCCE) approach¹⁹ was instead employed to calculate pK_a values of all 23 lysine residues in the cytosolic domain of the IRE1 (PDB/Chain ID: 3P23.A). MCCE combines continuum electrostatics and molecular mechanics.¹⁹ The protein side chain motions are simulated explicitly through rotamer sampling while the dielectric effect of the solvent and bulk protein is modeled by continuum electrostatics. The electrostatic interactions were computed by means of the Poisson–Boltzmann equation through multiple DelPhi runs as implemented into MCCE v2.7, and the resulting pK_a values were obtained using Metropolis Monte Carlo sampling of all conformers as a function of pH.¹⁹

To confirm the MCCE simulation results, Quantum Mechanics/Molecular Mechanics (QM/MM) calculations²¹ were performed to evaluate the explicit interaction between residues around K907 in the IRE1 RNase domain (residues 830–964).

Moreover, potential energy surface (PES) scans and hydrogen bond strength calculations were performed using the same approach.

Except for residue K907, for which the IRE1/MKC9989 covalent complex is available (PDB code: 4PL3),⁹ covalent docking²² was used in the absence of crystallographic structures to provide covalent IRE1/MKC9989 complexes with a total of four representative lysine residues.¹⁰ The stability and non-bonded interactions of the covalently bound MKC9989 inhibitor with two buried (K907 and K599) and two solvent accessible (K656 and K799) lysines (Fig. 1) were studied using a series of MD simulations.¹⁰ Also, the solvent accessibility of the newly formed imine groups, after Schiff base reaction, was quantitatively studied by means of radial distribution function (RDF) of water molecules around the imine groups during the MD simulation.

Upon combining the results of MCCE simulation, QM/MM calculations and MD simulations, the data in full explains the observed high selectivity of MKC9989 and related HAA-based inhibitors towards K907.¹⁰

2. Methods

2.1. Protein preparation

The IRE1 apo monomer was built by keeping chain A from the crystal structure (PDB ID: 4PL3)⁹ and removing all other chains, ligands and cofactors, including the covalently bound MKC9989. The residue involved in Schiff base formation, K907, was restored to its original lysine side chain form. The IRE1 apo monomer was then prepared using the protein preparation wizard implemented in the Schrödinger program package.²³ Hydrogen atoms were incorporated and possible missing side



chain atoms and missing loops were added using the Prime program.^{11,24} Tautomeric and protonation states of all residues were determined at pH = 7.4. The prepared structure of IRE1 was then refined using the OPLS3e force field²⁵ in a restrained minimization procedure.

2.2. MCCE simulation

The MCCE technique¹⁹ was employed to calculate pK_a values of all residues in the prepared IRE1 structure. All side chain atoms were allowed to move while the protein backbone was considered to be rigid. Also, all protonatable residues were allowed to be in neutral or ionized states. PARSE radii and charges were used for the protein atoms.²⁶ The MCCE simulations were carried out with three different protein dielectric constant values ($\epsilon = 2, 3,$ and 4), while the solvent dielectric constant was kept constant at 80 with a salt concentration of 150 mM. It has been demonstrated that a protein dielectric constant of 2 is consistent with PARSE charges^{27,28} and it is also commonly used for many studies based on Molecular Mechanics Poisson-Boltzmann (MM-PB)²⁹ or Molecular Mechanics Generalized Born (MM-GB)³⁰ methods. The value of ϵ used in a calculation depends on the level of physical detail represented explicitly in a model.³¹ For fully microscopic simulations, $\epsilon = 1$ because all contributions to dielectric relaxation in the protein-water system are treated explicitly.³² However, microscopic models of the system with implicit treatment of induced dipoles (electronic polarization) will be best described by using $\epsilon = 2$.³² On the other hand, when the both induced dipoles and protein relaxation (nuclear relaxation or reorientation of dipoles) are treated implicitly, $\epsilon > 4$ should be used.³³ In the MCCE simulation, protein relaxation is simulated explicitly through rotamer sampling while the dielectric effects of the solvent and bulk protein are modeled implicitly by continuum electrostatics. Therefore, according to literature, $\epsilon = 2$ can be an appropriate choice for dielectric constants of the protein.³⁴

The torsion energies and van der Waals parameters were evaluated based on the standard AMBER force field.³⁵ Herein, we employed FULL MCCE analysis where the positions of all side chains were first determined by (a) rotation around all rotatable bonds by 45° increments followed by (b) pruning rotamers with undesirable clashes. Afterwards, two step optimizations were carried out for dihedral angle optimization and for proton addition followed by final pruning of conformers. A total number of 7936, 7110, and 6467 conformers were considered for DelPhi³⁶ pairwise interaction calculations and Monte Carlo sampling procedure at $\epsilon = 2, 3,$ and 4 , respectively.

2.3. MKC9989 ligand preparation

The structure of the MKC9989 ligand was obtained from the co-crystallized PDB structure (4PL3) and its aldehyde moiety was re-modeled as appropriate (Fig. 1). The pre-reactive MKC9989 ligand was then prepared in the Schrödinger LigPrep program at pH = 7.4 using the OPLS3e force field.²⁵ Finally, the most stable conformer of the ligand was determined using the MacroModel program implemented in the Schrödinger suite, and used for covalent docking studies. Herein, we used the Mixed

Torsional/Low-Mode sampling (MTLMD) method.³⁷ The probability of torsion rotation/molecular translation was set to 0.5 with 100 steps per rotated bond. The minimum and maximum distances for low-mode motions were set to 3.0 and 6.0 Å, respectively. The energy window for saving the structures and maximum atom deviation cutoff were assigned to be 5.0 kcal mol⁻¹ and 0.5 Å, respectively. The OPLS3e force field was employed with water as solvent. The extended cutoff option was chosen to truncate the non-covalent interactions (*i.e.* 8.0, 20.0, and 4.0 Å for van der Waals, electrostatic, and hydrogen bond interactions, respectively). The Polak-Ribiere conjugate gradient (PRCG)³⁸ method with maximum iteration of 2500 and convergence threshold of 0.05 kJ mol⁻¹ Å⁻¹ was used as minimization algorithm acting on the gradient.

2.4. Covalent docking

Besides the co-crystallized complex with MKC9989 covalently bound to K907, the prepared MKC9989 ligand was covalently docked into IRE1 using CovDock in Schrödinger.³⁹ The additional selected lysine residues (K599, K656 and K799) were defined as active residues and the imine condensation reaction between the amine group of the lysine and the reactive aldehyde of MKC9989 was simulated. Energies were calculated using the MM-GBSA rescoring function.⁴⁰ As described in ref. 10, by performing Solvent Accessible Surface Area (SASA) analysis of the twenty-three lysine residues in the IRE1 cytosolic domain, two representative buried lysines (*i.e.* K907 and Lys599) and two solvent exposed lysines (*i.e.* K656 and K799) have been chosen. The calculated SASA values are 6.1, 11.5, 104.0, and 200.0 Å² for K907, K599, K799, and K656, respectively. The general idea was to choose representative lysines in a way that they are at a distance from each other to avoid ligand-ligand interactions and minimize allosteric effects during the IRE1 + 4 MKC9989 MD simulations (Fig. 1).

2.5. MD simulation

The highest scoring poses from the covalent docking at each of the three additional lysines were, together with the K907-bound crystallographic structure, subjected to an MD simulation in NPT ensemble using the Desmond MD simulator engine in Schrödinger⁴¹ employing the OPLS3e force field.²⁵ Water molecules were modeled using the TIP3P force field.⁴² Periodic boundary conditions were applied in all directions along with a 10 Å water buffer around the protein in an orthorhombic simulation box. The net charge of the system was balanced using the proper number of counter ions (*i.e.* Cl⁻/Na⁺) and the salt concentration was set to 150 mM to represent physiological conditions. Temperature (300 K) and pressure (1 atm) were controlled using the Nose-Hoover thermostat⁴³ and the Martyna-Tobias-Klein barostat,⁴⁴ respectively. The initial minimization and relaxation protocol consisted of (a) NVT Brownian dynamics with restraints on solute heavy atoms at $T = 10$ K for 100 ps, (b) NVT simulation at $T = 10$ K with restraints on solute heavy atoms for 12 ps, (c) NPT MD simulation at $T = 10$ K with restraints on solute heavy atoms for 12 ps, (d) NPT MD simulation at $T = 300$ K with restraints on solute heavy atoms for 12



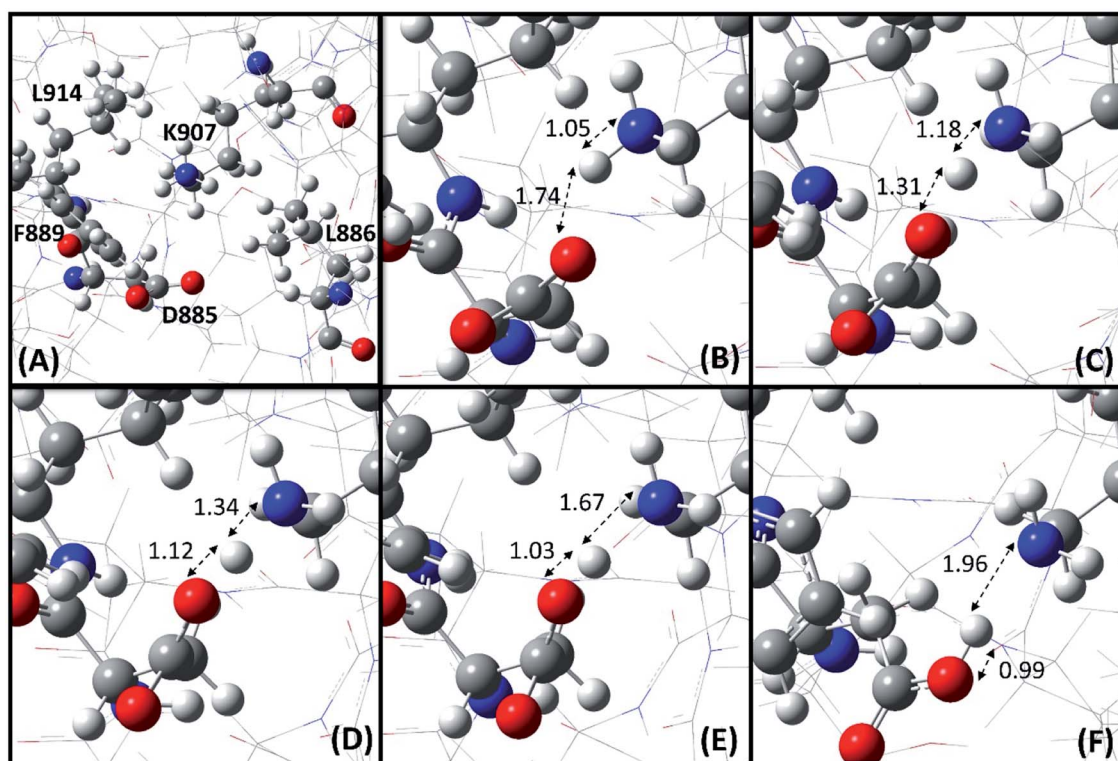


Fig. 2 Proton transfer from K907 to D885 during the structure optimization. (A) Initial configuration (step #1), and zoomed in at (B) step #15, (C) step #25, (D) step #35, (E) step #45, and (F) optimized configuration (step #352). The NH and OH bond lengths are in Å. Oxygen, nitrogen, carbon and hydrogen atoms are shown as red, blue, gray and white spheres, respectively.

ps, and (e) NPT MD simulation at $T = 300$ K without restraints for 24 ps. Following equilibration, the MD simulation was then run for 100 ns with a trajectory sampling frequency of 100 ps in the production step.

2.6. QM/MM calculations

The ONIOM (Our own N-layered Integrated molecular Orbital and molecular Mechanics) technique,⁴⁵ as implemented in Gaussian 16,⁴⁶ was employed to carry out the QM/MM calculations on the RNase domain of IRE1 (residues 830–964). The residues K907, D885, F889, L886 and L914 (Fig. 2A) were considered as the QM region and treated by the dispersion corrected Minnesota M06-2X functional⁴⁷ along with the 6-31+G(d,p) basis set, while the rest of the RNase domain was assigned as the MM region for which the Universal Force Field (UFF)⁴⁸ was employed. The structure optimization started with ionized states of K907 and D885. The potential energy surface (PES) scan and hydrogen bond strength evaluation were performed at the same level of theory. The PES scan was performed as a function of OH distance (0.7–2.2 Å with step length 0.1 Å) and OHN angle ($180 \pm 75^\circ$).

3. Results and discussion

3.1. Pre-Schiff base reaction analysis

Fig. 3 shows the pK_a values of all lysine residues extracted from the MCCE simulations at protein dielectric constants 2, 3, and

4. The lowest pK_a values belong to K907 and K559 with values 8.6, 5.1, and 0.7 (K907) and 9.0, 8.4, and 7.6 (K559) at $\epsilon = 4, 3,$ and 2, respectively. The pK_a values of these two buried residues decrease as ϵ decreases which indicates their preferences to be deprotonated at lower protein dielectric constants. It is surprising that pK_a of K907 at $\epsilon = 2$ is totally acidic compared to the other lysine residues (Fig. 3). The pK_a values of the remaining lysines are essentially unaffected by the change in dielectric constant, and range between 8 and 12.5. A closer look at the pK_a values of the other residues around K907 (Fig. 2A) indicates that D885 exerts an equally abnormal increase in pK_a with decreasing protein dielectric constant. The pK_a values of D885 are calculated to be 1.8, 3.5, and 9.6 at $\epsilon = 4, 3,$ and 2, respectively. This result clearly illustrates an interaction between K907 and D885 inside the hydrophobic cavity, which is significantly enhanced as the protein dielectric constant is reduced.

It has been demonstrated that the pK_a of a buried ionizable residue is extremely sensitive to the protein conformation and polarity of the surrounding microenvironment.¹⁷ In internal polar hydrophilic microenvironments, the pK_a values are close to those of individual amino acids in water. However, in apolar hydrophobic microenvironments, the pK_a of ionizable residues will shift making the neutral state more favorable.¹⁷ Isom *et al.* have studied the effect of the polarity of the microenvironment on the pK_a of lysine residues by engineering 25 variants of staphylococcal nuclease with lysine residues at internal



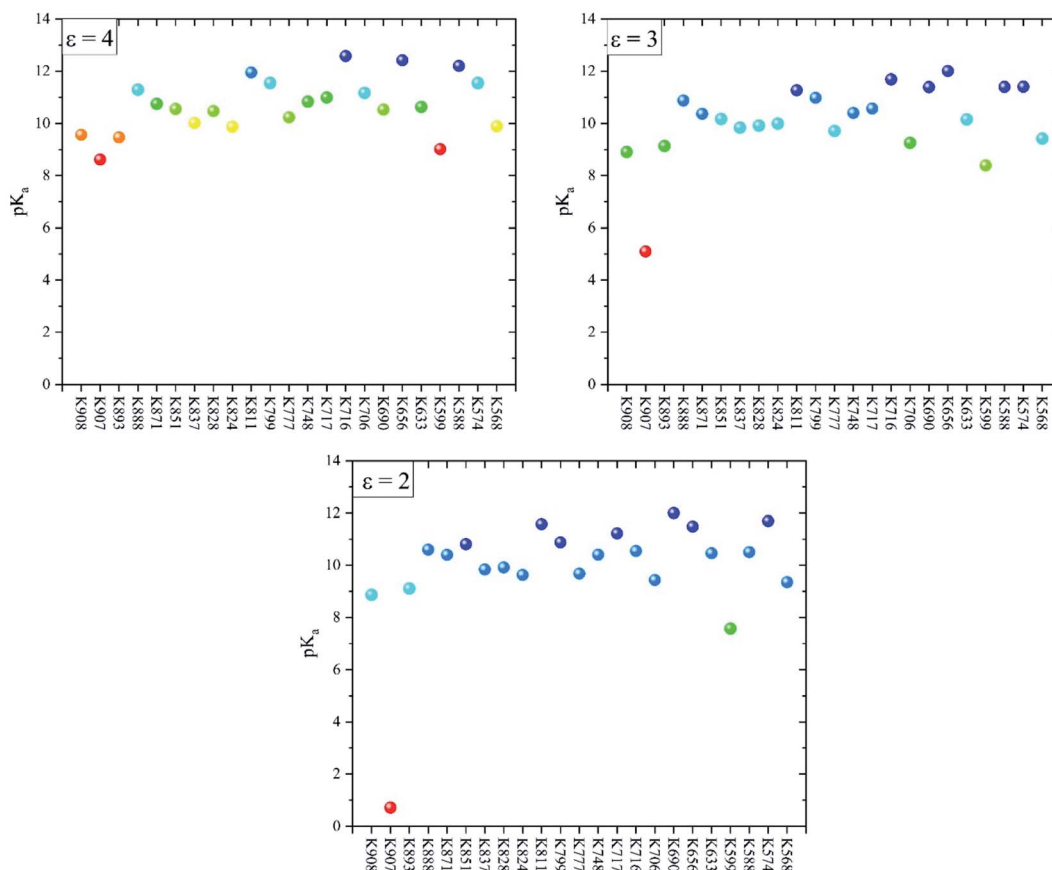


Fig. 3 The calculated pK_a values of all 23 Lys residues of the IRE1 cytosolic domain at three different protein dielectric constants (i.e. $\epsilon = 4, 3,$ and 2). Intermediate residues colored relative to the lowest (red) and highest (blue) value in each set.

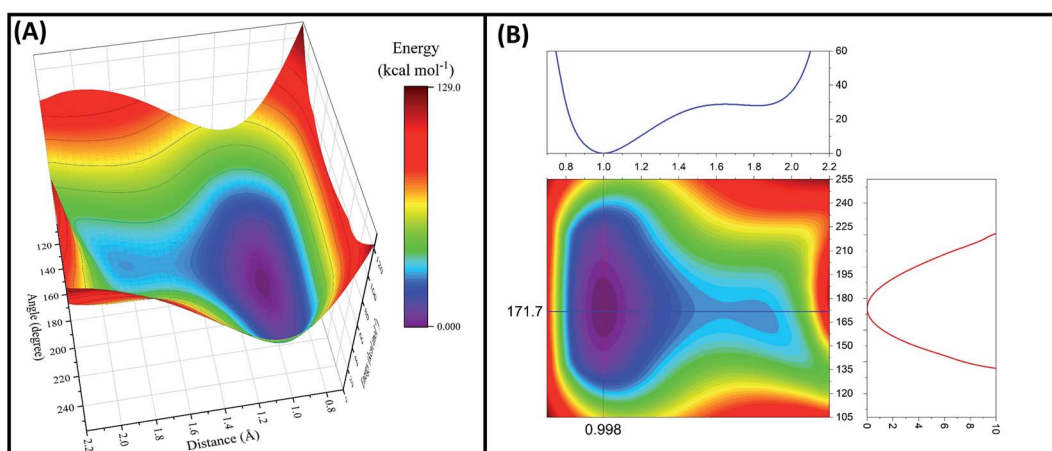


Fig. 4 The PES (kcal mol^{-1}) along the proton transfer pathway from K907 to D885. (A) 3D PES as a function of OH distance (\AA) and OHN angle (degrees). (B) Contour map profile of PES with optimum values of OH bond and OHN angle depicted with straight blue and red lines, respectively.

positions.¹⁷ They found a very large reduction in pK_a of some lysine residues, as low as 5.3, inside a hydrophobic pocket in close proximity to carboxylic group containing residues.

To confirm the MCCE results and to investigate the interaction between K907 and the surrounding residues, a series of

QM/MM calculation were conducted based on dispersion corrected DFT using the M06-2X functional. We started the structure optimization process with K907 and D885 in their respective ionized states, based on the prepared pdb structure (PDB code: 4PL3). As Fig. 2 shows, a clear proton transfer occurs



from K907 to D885 during the optimization. This implies that K907 prefers to remain deprotonated inside the highly hydrophobic pocket surrounded by F889, L886, and L914. The transferred proton maintains a hydrogen bond between the donor and acceptor atoms in the optimized structure, with OH, NH, and ON distances 0.99, 1.96, and 2.95 Å, respectively, and OHN angle 171.8°. Additional calculations revealed that this hydrogen bond is relatively weak, with an energy of 10.1 kcal mol⁻¹.

Since the proton transfer has occurred during the structure optimization process, it is expected that there is no or very low energy barrier for this reaction mechanism. Indeed, a PES scan, performed as a function of OH distance (0.7–2.2 Å with step length 0.1 Å) and OHN angle (180 ± 75°), confirms the hypothesis (Fig. 4). As seen in Fig. 4A, the PES along the proton transfer pathway possesses a double minimum profile feature with a very shallow well around the amine nitrogen atom of K907 residue. Indeed, the energy barrier for proton transfer from K907 to D885 (0.82 kcal mol⁻¹) is 35 times lower than the proton transfer in the opposite direction (28.89 kcal mol⁻¹). This very small energy barrier could not prohibit the spontaneous proton transfer during the optimization as it is close to the RT value at 298 K (~0.6 kcal mol⁻¹); *i.e.* the proton will easily pass through this minimal barrier just by means of thermal motion. Two main phenomena explain how proton transfer can occur during the minimization: (1) strong electrostatic interaction of positively charged K907 and negatively charged D885 leads to an enhancement in zero-point vibrational energy and amplitude of N–H vibration, which consequently can overcome the small energy barrier. (2) It is well-known that, due to light weight of the proton, quantum effects cannot be neglected for reactions involving proton transfer.⁴⁹ Proton tunneling is a quantum mechanical phenomenon that can justify how

Table 1 Docking score and MM-GBSA free energy of binding (ΔG_b) of MKC9989 to the different sites of IRE1

Docking site	Docking score	MM-GBSA ΔG_b (kcal mol ⁻¹)
K599	-4.61	-38.04
K656	-3.18	Not reported ^a
K799	-3.73	Not reported ^a
K907	-5.90	-61.12

^a Not reported by CovDock program.

protons can transfer from one microstate to another one by passing through the energy barrier between the two.⁴⁹

The contour map profile of the PES (Fig. 4B) shows that the optimum values for OH distance and OHN angle are 0.998 Å and 171.7° which are consistent with the structural parameters of the optimized configuration. The results of the pK_a calculations from the MCCE simulations and the spontaneous proton transfer phenomenon from the QM/MM calculations provide a clear picture linking the prerequisites for Schiff base chemical reaction to the high selectivity of MKC9989 towards K907.

3.2. Post-Schiff base reaction analysis

To investigate the parameters which may influence the stability of the newly formed Schiff base between four representative lysine residues¹⁰ and the aldehyde moiety of MKC9989, the covalent complexes between MKC9989 and K599 (kinase pocket), K656 and K799 (solvent exposed), and K907 (RNase site), were explored further (Fig. 5). The docking score values and MM-GBSA free energy of binding (ΔG_b) (Table 1) indicate that the pocket containing K907 is the favored site for covalently bound MKC9989 to IRE1. However, given the difficulty of the

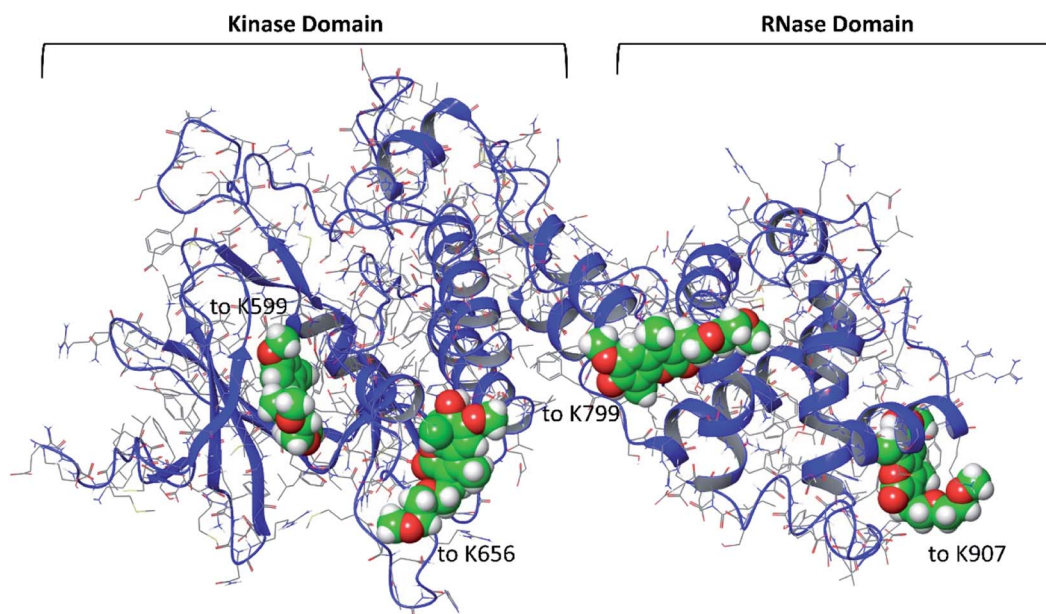


Fig. 5 The structure of the four covalently bound MKC9989 molecules (space filling model) to the four selected lysine residues of the cytosolic part of IRE1.



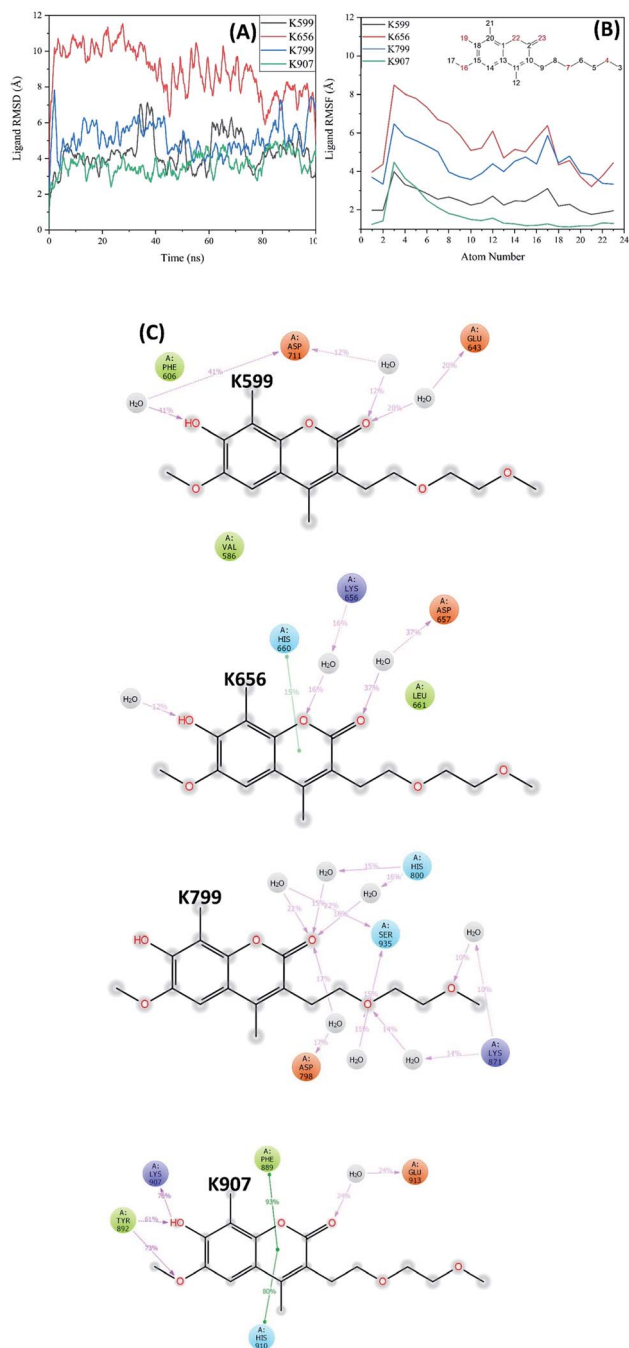


Fig. 6 (A) RMSD of MKC9989 ligands covalently attached to the different lysine residues during the 100 ns MD simulation. (B) RMSF plot of MKC9989 ligands covalently bound to the different lysine residues during the MD simulation. The atom numbers are according to the 2D structure of the ligand shown in the inset panel. (C) Protein–ligand interaction diagrams for MKC9989 attached to the different lysine residues. Abundance of interactions (% of MD simulation trajectory snapshots), and solvent exposure of the ligand atoms (grey spheres) are also displayed.

CovDock program to reproduce the exact crystallographic pose of MKC9989 towards K907,⁵⁰ we decided to use the structure from PDB ID 4PL3 at this particular site in the further investigations.

The IRE1/4×MKC9989 complex was then subjected to a 100 ns MD simulation for further evaluation of ligand dynamics and solvent accessibility of the formed imine bond. As mentioned, solvent accessibility is an important parameter since the imine group can easily be hydrolyzed in the presence of water molecules in a reverse Schiff base reaction. Fig. 6A shows the RMSD of the covalently attached MKC9989 ligands during the 100 ns molecular dynamics simulation. As this figure indicates, the ligand movement inside the RNase pocket (K907) is smaller compared to the MKC9989 ligands covalently bound to K599, K656 and K799.

Fig. 6B shows the RMSF plot of the ligand bound to the four different lysines. Ligand RMSF plots describe the ligand fluctuations broken down to individual atoms. The atom numbers are according to the 2D structure of the ligand shown in the inset panel of Fig. 6B. The ligand RMSF will give us better insight on how ligand fragments interact with the protein and their entropic role during the binding event. As the figure indicates, the RMSF values of the ligand bound to K907 are considerably lower than those attached to the other lysines (specifically solvent exposed ones). The differences in RMSF values are significant for atoms around the covalent bonding position (*i.e.* two fused rings) which confirms the stability of MKC9989 bound to K907 within the RNase domain.

The protein–ligand interaction diagram (Fig. 6C) shows that MKC9989 inside the pocket containing K907 exhibits π – π interactions with F889 and H910 during 90% and 83% of the simulation time, respectively. The very low solvent accessibility of the imine group formed within this region (Fig. 7) can be associated to these π – π interactions that prevent water molecules from diffusing into the pocket and make, along with the strong hydrogen bonds to Y892 and K907, the ligand molecule more rigidly bound inside this pocket in comparison with the other sites (Fig. 6B). Common for MKC9989 bound to any of the other three lysines are water-assisted hydrogen bonds to the interacting residues, and a high degree of solvent exposure.

In Fig. 7A we present the radial distribution function, RDF ($g(r)$), of water molecules around each imine groups as a function of distance between the carbon atom of the imine (C_i) and oxygen atoms of water (O_w) during the MD simulation. The lack of the first peak in the RDF plot of MKC9989 inside the pocket containing K907 shows that the corresponding imine group is fully inaccessible to water molecules, which prevents imine hydrolysis process from taking place. Fig. 7B shows the integral of RDF during the MD simulation which quantitatively represents the average number of water molecules around each imine groups, as a function of distance. As Fig. 7B indicates, as opposed to the other three lysines, there are no water molecules around the imine group formed during the reaction between MKC9989 and K907, up to 6 Å away from the C_i atom. As discussed earlier, the strong π – π interactions between MKC9989 and F889 and H910 may block the water molecules from diffusing into the pocket region.



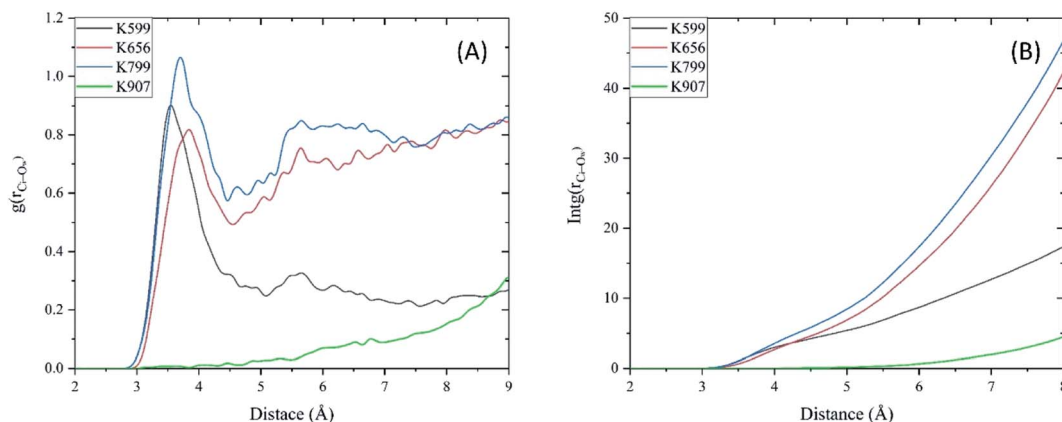


Fig. 7 (A) RDF of water molecules, and (B) average number of water molecules (integral of RDF) around each imine group as a function of distance between the carbon atom of the imine (C_i) and oxygen atoms of water (O_w) during the MD simulations.

4. Conclusions

Herein, the high selectivity of the UPR inhibitor MKC9989 towards K907 in the IRE1 RNase pocket is investigated by means of multiscale *in silico* techniques including MCCE simulations, QM/MM calculations, covalent docking, and MD simulations. The MCCE simulations showed that the lowest pK_a values belong to K907 and K559 with values of 8.6 and 9.0, 5.1 and 8.4, and 0.7 and 7.6 at $\epsilon = 4, 3$, and 2, respectively. The pK_a values of in particular K907 decreases dramatically as ϵ decreases, which indicates preferred deprotonation at lower protein dielectric constants. The MCCE simulations also identified a critical interaction between K907 and D885 within the hydrophobic pocket, which was markedly enhanced at lower protein dielectric constants. The QM/MM calculations showed a spontaneous proton transfer from K907 to D885, in agreement with the low pK_a value of the K907 residue. The PES scan confirmed the negligible energy barrier (0.82 kcal mol⁻¹) associated with this proton transfer reaction. The results from covalent docking and MD simulations demonstrated that the pocket containing K907 can effectively stabilize the inhibitor's structure by strong π - π and hydrogen bonding interactions. RDF analyses furthermore confirmed that the imine group formed in the chemical reaction between MKC9989 and K907 is totally inaccessible for water molecules, and thus the probability of imine hydrolysis is negligible.

These results give new insights into the selectivity of the MKC9989 inhibitor towards K907 out of the 23 lysine residues of IRE1, and provide a suitable starting point for QM/MM or QM/MM-MD studies of the MKC9989-IRE1 reaction. This work also shows how different computational tools can be utilized to describe the local factors leading to Schiff base formation in biological systems.

Authors contributions

All authors conceived the study. S. J. M. performed the computations, analyzed the data and wrote the first draft. All authors revised the text.

Data availability

All simulation protocols, input files for QM/MM and MCCE calculations, and output structures from covalent docking are provided as tarballs (.tar.gz) freely accessible at zenodo.org as DOI: 10.5281/zenodo.3621358.

Conflicts of interest

The authors declare no conflicting interests.

Acknowledgements

This research was funded by the EU's Horizon 2020 research and innovation programme under the Marie Skłodowska-Curie grant 675448 (TRAINERS) and MSCA-RISE-734749 (INSPIRED). Funding from the Vinnova Seal-of-Excellence programme 2019-02205 (CaTheDRA) is gratefully acknowledged (S. J. M.). The Faculty of Science at the University of Gothenburg and the Swedish Science Research Council (VR; grant number 2019-3684) are gratefully acknowledged for financial support (L. A. E.) and the Swedish National Infrastructure for Computing for allocations of computing time at supercomputing center C3SE.

References

- C. E. Shamu and P. Walter, Oligomerization and phosphorylation of the Ire1p kinase during intracellular signaling from the endoplasmic reticulum to the nucleus, *EMBO J.*, 1996, **15**(12), 3028–3039.
- H. Yoshida, T. Matsui, A. Yamamoto, T. Okada and K. Mori, XBP1 mRNA is induced by ATF6 and spliced by IRE1 in response to ER stress to produce a highly active transcription factor, *Cell*, 2001, **107**(7), 881–891.
- Y. Lu, F.-X. Liang and X. Wang, A synthetic biology approach identifies the mammalian UPR RNA ligase RtcB, *Mol. Cell*, 2014, **55**(5), 758–770.
- S. G. Kosmaczewski, T. J. Edwards, S. M. Han, M. J. Eckwahl, B. I. Meyer, S. Peach, J. R. Hesselberth, S. L. Wolin and



- M. Hammarlund, The RtcB RNA ligase is an essential component of the metazoan unfolded protein response, *EMBO Rep.*, 2014, **15**(12), 1278–1285.
- 5 M. Calfon, H. Zeng, F. Urano, J. H. Till, S. R. Hubbard, H. P. Harding, S. G. Clark and D. Ron, IRE1 couples endoplasmic reticulum load to secretory capacity by processing the XBP-1 mRNA, *Nature*, 2002, **415**(6867), 92.
- 6 D. Doultsinos, T. Avril, S. Lhomond, N. Dejeans, P. Guédat and E. Chevet, Control of the unfolded protein response in health and disease, *SLAS Discov.*, 2017, **22**(7), 787–800.
- 7 B. C. Cross, P. J. Bond, P. G. Sadowski, B. K. Jha, J. Zak, J. M. Goodman, R. H. Silverman, T. A. Neubert, I. R. Baxendale and D. Ron, The molecular basis for selective inhibition of unconventional mRNA splicing by an IRE1-binding small molecule, *Proc. Natl. Acad. Sci. U.S.A.*, 2012, **109**(15), E869–E878.
- 8 S. M. Tomasio, H. P. Harding, D. Ron, B. C. Cross and P. J. Bond, Selective inhibition of the unfolded protein response: targeting catalytic sites for Schiff base modification, *Mol. BioSyst.*, 2013, **9**(10), 2408–2416.
- 9 M. Sanches, N. M. Duffy, M. Talukdar, N. Thevakumaran, D. Chiovitti, M. D. Canny, K. Lee, I. Kurinov, D. Uehling and R. Al-Awar, Structure and mechanism of action of the hydroxy-aryl-aldehyde class of IRE1 endoribonuclease inhibitors, *Nat. Commun.*, 2014, **5**, 4202.
- 10 A. Carlesso and L. A. Eriksson, Selective Inhibition of IRE1 Signalling Mediated by MKC9989: New Insights from Molecular Docking and Molecular Dynamics Simulations, *ChemistrySelect*, 2019, **4**(11), 3199–3203.
- 11 M. P. Jacobson, R. A. Friesner, Z. Xiang and B. Honig, On the role of the crystal environment in determining protein side-chain conformations, *J. Mol. Biol.*, 2002, **320**(3), 597–608.
- 12 L. A. Highbarger, J. A. Gerlt and G. L. Kenyon, Mechanism of the reaction catalyzed by acetoacetate decarboxylase. Importance of lysine 116 in determining the pK_a of active-site lysine 115, *Biochemistry*, 1996, **35**(1), 41–46.
- 13 A. Stank, D. B. Kokh, J. C. Fuller and R. C. Wade, Protein binding pocket dynamics, *Acc. Chem. Res.*, 2016, **49**(5), 809–815.
- 14 M. Ciaccia and S. Di Stefano, Mechanisms of imine exchange reactions in organic solvents, *Org. Biomol. Chem.*, 2015, **13**(3), 646–654.
- 15 J. Reijenga, A. van Hoof, A. van Loon and B. Teunissen, Development of methods for the determination of pK_a values, *Anal. Chem. Insights*, 2013, **8**, S12304.
- 16 M. Gunner, X. Zhu and M. C. Klein, MCCE analysis of the pK_a s of introduced buried acids and bases in staphylococcal nuclease, *Proteins: Struct., Funct., Bioinf.*, 2011, **79**(12), 3306–3319.
- 17 D. G. Isom, C. A. Castañeda and B. R. Cannon, Large shifts in pK_a values of lysine residues buried inside a protein, *Proc. Natl. Acad. Sci. U.S.A.*, 2011, **108**(13), 5260–5265.
- 18 J. Antosiewicz, J. A. McCammon and M. K. Gilson, Prediction of pH-dependent properties of proteins, *J. Mol. Biol.*, 1994, **238**(3), 415–436.
- 19 Y. Song, J. Mao and M. Gunner, MCCE2: improving protein pK_a calculations with extensive side chain rotamer sampling, *J. Comput. Chem.*, 2009, **30**(14), 2231–2247.
- 20 E. Alexov, Calculating proton uptake/release and binding free energy taking into account ionization and conformation changes induced by protein-inhibitor association: application to plasmepsin, cathepsin D and endothiasepsin-pepstatin complexes, *Proteins: Struct., Funct., Bioinf.*, 2004, **56**(3), 572–584.
- 21 H. M. Senn and W. Thiel, QM/MM methods for biological systems, in *Atomistic approaches in modern biology*, Springer, 2006, pp. 173–290.
- 22 H. Kumalo, S. Bhakat and M. Soliman, Theory and applications of covalent docking in drug discovery: merits and pitfalls, *Molecules*, 2015, **20**(2), 1984–2000.
- 23 G. M. Sastry, M. Adzhigirey, T. Day, R. Annabhimoju and W. Sherman, Protein and ligand preparation: parameters, protocols, and influence on virtual screening enrichments, *J. Comput. Aided Mol. Des.*, 2013, **27**(3), 221–234.
- 24 M. P. Jacobson, D. L. Pincus, C. S. Rapp, T. J. Day, B. Honig, D. E. Shaw and R. A. Friesner, A hierarchical approach to all-atom protein loop prediction, *Proteins: Struct., Funct., Bioinf.*, 2004, **55**(2), 351–367.
- 25 K. Roos, C. Wu, W. Damm, M. Reboul, J. M. Stevenson, C. Lu, M. K. Dahlgren, S. Mondal, W. Chen and L. Wang, OPLS3e: extending force field coverage for drug-like small molecules, *J. Chem. Theor. Comput.*, 2019, **15**(3), 1863–1874.
- 26 D. Sitkoff, K. A. Sharp and B. Honig, Accurate calculation of hydration free energies using macroscopic solvent models, *J. Phys. Chem.*, 1994, **98**(7), 1978–1988.
- 27 K. Sharp, A. Jean-Charles and B. Honig, A local dielectric constant model for solvation free energies which accounts for solute polarizability, *J. Phys. Chem.*, 1992, **96**(9), 3822–3828.
- 28 P. Barth, T. Alber and P. Harbury, Accurate, conformation-dependent predictions of solvent effects on protein ionization constants, *Proc. Natl. Acad. Sci. U.S.A.*, 2007, **104**(12), 4898–4903.
- 29 R. Kong, T. Liu, X. Zhu, S. Ahmad, A. L. Williams, A. T. Phan, H. Zhao, J. E. Scott, L.-A. Yeh and S. T. Wong, Old drug new use—amoxapine and its metabolites as potent bacterial β -glucuronidase inhibitors for alleviating cancer drug toxicity, *Clin. Cancer Res.*, 2014, **20**(13), 3521–3530.
- 30 P. A. Kollman, I. Massova, C. Reyes, B. Kuhn, S. Huo, L. Chong, M. Lee, T. Lee, Y. Duan and W. Wang, Calculating structures and free energies of complex molecules: combining molecular mechanics and continuum models, *Acc. Chem. Res.*, 2000, **33**(12), 889–897.
- 31 C. N. Schutz and A. Warshel, What are the dielectric “constants” of proteins and how to validate electrostatic models?, *Proteins: Struct., Funct., Bioinf.*, 2001, **44**(4), 400–417.
- 32 C. A. Fitch, D. A. Karp, K. K. Lee, W. E. Stites, E. E. Lattman and E. B. García-Moreno, Experimental pK_a values of buried residues: analysis with continuum methods and role of water penetration, *Biophys. J.*, 2002, **82**(6), 3289–3304.



- 33 T. Simonson, G. Archontis and M. Karplus, A Poisson–Boltzmann study of charge insertion in an enzyme active site: the effect of dielectric relaxation, *J. Phys. Chem. B*, 1999, **103**(29), 6142–6156.
- 34 H. Park and Y. H. Jeon, Cubic equation governing the outer-region dielectric constant of globular proteins, *Phys. Rev. E*, 2007, **75**(2), 021916.
- 35 W. D. Cornell, P. Cieplak, C. I. Bayly, I. R. Gould, K. M. Merz, D. M. Ferguson, D. C. Spellmeyer, T. Fox, J. W. Caldwell and P. A. Kollman, A second generation force field for the simulation of proteins, nucleic acids, and organic molecules, *J. Am. Chem. Soc.*, 1995, **117**(19), 5179–5197.
- 36 B. Honig, K. Sharp and A. S. Yang, Macroscopic models of aqueous solutions: biological and chemical applications, *J. Phys. Chem.*, 1993, **97**(6), 1101–1109.
- 37 D. K. Agrafiotis, A. C. Gibbs, F. Zhu, S. Izrailev and E. Martin, Conformational sampling of bioactive molecules: a comparative study, *J. Chem. Inf. Model.*, 2007, **47**(3), 1067–1086.
- 38 L. Grippo and S. Lucidi, A globally convergent version of the Polak-Ribiere conjugate gradient method, *Math. Program.*, 1997, **78**(3), 375–391.
- 39 K. Zhu, K. W. Borrelli, J. R. Greenwood, T. Day, R. Abel, R. S. Farid and E. Harder, Docking covalent inhibitors: a parameter free approach to pose prediction and scoring, *J. Chem. Inf. Model.*, 2014, **54**(7), 1932–1940.
- 40 G. Rastelli, A. D. Rio, G. Degliesposti and M. Sgobba, Fast and accurate predictions of binding free energies using MM-PBSA and MM-GBSA, *J. Comput. Chem.*, 2010, **31**(4), 797–810.
- 41 K. J. Bowers, D. E. Chow, H. Xu, R. O. Dror, M. P. Eastwood, B. A. Gregersen, J. L. Klepeis, I. Kolossvary, M. A. Moraes and F. D. Sacerdoti, Scalable algorithms for molecular dynamics simulations on commodity clusters, SC'06, in *Proceedings of the 2006 ACM/IEEE Conference on Supercomputing*, IEEE, 2006, pp. 43–43.
- 42 W. L. Jorgensen, J. Chandrasekhar, J. D. Madura, R. W. Impey and M. L. Klein, Comparison of simple potential functions for simulating liquid water, *J. Chem. Phys.*, 1983, **79**(2), 926–935.
- 43 G. J. Martyna, M. L. Klein and M. Tuckerman, Nosé–Hoover chains: the canonical ensemble *via* continuous dynamics, *J. Chem. Phys.*, 1992, **97**(4), 2635–2643.
- 44 R. M. Wentzcovitch, Invariant molecular-dynamics approach to structural phase transitions, *Phys. Rev. B: Condens. Matter Mater. Phys.*, 1991, **44**(5), 2358.
- 45 T. Vreven, K. S. Byun, I. Komáromi, S. Dapprich, J. A. Montgomery Jr, K. Morokuma and M. J. Frisch, Combining quantum mechanics methods with molecular mechanics methods in ONIOM, *J. Chem. Theory Comput.*, 2006, **2**(3), 815–826.
- 46 M. J. Frisch; G. W. Trucks; H. B. Schlegel; G. E. Scuseria; M. A. Robb; J. R. Cheeseman; G. Scalmani; V. Barone; G. A. Petersson; H. Nakatsuji; X. Li; M. Caricato; A. V. Marenich; J. Bloino; B. G. Janesko; R. Gomperts; B. Mennucci; H. P. Hratchian; J. V. Ortiz; A. F. Izmaylov; J. L. Sonnenberg; D. Williams-Young; F. Ding; F. Lipparini; F. Egidi; J. Goings; B. Peng; A. Petrone; T. Henderson; D. Ranasinghe; V. G. Zakrzewski; J. Gao; N. Rega; G. Zheng; W. Liang; M. Hada; M. Ehara; K. Toyota; R. Fukuda; J. Hasegawa; M. Ishida; T. Nakajima; Y. Honda; O. Kitao; H. Nakai; T. Vreven; K. Throssell; J. A. Montgomery Jr; J. E. Peralta; F. Ogliaro; M. J. Bearpark; J. J. Heyd; E. N. Brothers; K. N. Kudin; V. N. Staroverov; T. A. Keith; R. Kobayashi; J. Normand; K. Raghavachari; A. P. Rendell; J. C. Burant; S. S. Iyengar; J. Tomasi; M. Cossi; J. M. Millam; M. Klene; C. Adamo; R. Cammi; J. W. Ochterski; R. L. Martin; K. Morokuma; O. Farkas; J. B. Foresman; D. J. Fox, *Gaussian 16, Revision A.03*, Gaussian, Inc., Wallingford CT, 2016.
- 47 Y. Zhao and D. G. Truhlar, The M06 suite of density functionals for main group thermochemistry, thermochemical kinetics, noncovalent interactions, excited states, and transition elements: two new functionals and systematic testing of four M06-class functionals and 12 other functionals, *Theor. Chem. Acc.*, 2008, **120**(1–3), 215–241.
- 48 A. K. Rappé, C. J. Casewit, K. Colwell, W. A. Goddard III and W. M. Skiff, UFF, a full periodic table force field for molecular mechanics and molecular dynamics simulations, *J. Am. Chem. Soc.*, 1992, **114**(25), 10024–10035.
- 49 B. Salna, A. Benabbas, J. T. Sage, J. van Thor and P. M. Champion, Wide-dynamic-range kinetic investigations of deep proton tunnelling in proteins, *Nat. Chem.*, 2016, **8**(9), 874.
- 50 A. Carlesso, C. Chintia, A. M. Gorman, A. Samali and L. A. Eriksson, Merits and pitfalls of conventional and covalent docking in identifying new hydroxyl aryl aldehyde like compounds as human IRE1 inhibitors, *Sci. Rep.*, 2019, **9**(1), 3407.

